ADVANCED OPTICAL MATERIALS
www.advopticalmat.de

Engineering Core Size of InP Quantum Dot with Incipient ZnS for Blue Emission

Yo-Han Suh, Sanghyo Lee, Sung-Min Jung, Sang Yun Bang, Jiajie Yang, Xiang-Bing Fan, Shijie Zhan, Chatura Samarakoon, Jeong-Wan Jo, Yoonwoo Kim, Hyung Woo Choi, Luigi G. Occhipinti, Tae Hoon Lee, Dong-Wook Shin,* and Jong Min Kim*

Blue indium phosphide quantum dot (InP QD) is an emerging colloidal semiconductor nanocrystal, considered as a promising next-generation photoactive material for light-emitting purposes. Despite the tremendous progress in blue InP QDs, the synthetic method for tailoring InP core size to realize the blue-emissive QDs still lags behind. This work suggests a synthetic method for blue-emitting InP QDs by engineering the core size with an incipient ZnS (i-ZnS) shell. The formation of i-ZnS complexes, before the tris(trimethylsilyl) phosphine injection (e.g., before core growth process), restrains the overgrowth of InP nuclei by rapidly forming a ZnS shell on its surface, thereby resulting in further dwarfed InP cores. With additional ZnS shell coating, the blue QDs exhibit a photoluminescence quantum yield of ≈52% at 483 nm. The origin of bandgap diminution with the increase of shell thickness, or with the utilization of ZnSe shell is unraveled via the first-principles density functional theory simulations. Simulational evidence on InP-core densification with the shell coating, along with accompanying changes in chemical and structural properties, is presented. The blue-emitting InP QD device shows a maximum luminance of 1162 cd m^{-2} and external quantum efficiency of 1.4%.

1. Introduction

The enormous interest in the indium phosphide (InP)-based quantum dot (QD) has been globally maximized, because of the environmentally friendly constituent elements (lower toxicity), outstanding size-dependent monochromaticity, bandgap tunability, and high photoluminescence quantum yield (PLQY).[1–3] InP QDs have been considered as ideal alternative materials to toxic Cd-containing QDs for a wide range of applications such as light-emitting diodes (LEDs), lasers, solar cells, bio-maker, and sensors.[4–7] Breakthroughs in materials and synthetic-process development for highly luminescent InP QDs (green and red) have enabled the highest optical efficiencies reaching PLQY of 95%[8] and 100%,[9] respectively, comparable to the high-performance Cd-based QDs.

Blue InP QDs are regarded as breakthrough materials for an ideal future QD-based display.[10] Since 2008,[11] intensive efforts on the synthesis of blue InP QDs have been made. In particular, the high reactivity between tris(trimethylsilyl)phosphine (TMSP) and indium precursors allowed to form a magic-sized cluster as an intermediate, which enabled a uniform InP core formation with tunable emission wavelengths in the blue color region.[12,13] In 2008, the first step forward in the synthesis of blue InP@ZnS QDs (20% PLQY at 480 nm) was demonstrated using zinc carboxylate complexes that facilitate the stabilization of nanocrystal surfaces and the reduction of critical nuclei size during the growth of InP core.[11,14] Similar observations for the same QD materials were also reported in 2012 (36% PLQY at 430 nm)[15] and 2017 (44% PLQY at 488 nm).[16] Besides, size reduction of grown InP cores by acetic acid (a by-product of core growth process with TMSP at 150 °C) enabled the emission in the blue wavelength region (5% and 10% PLQYs at 475 and 485 nm, respectively).[17] InPZnS alloys grown with a long injection of TMSP[18] were also demonstrated with 24.5% PLQY at 495 nm. However, despite the tremendous efforts on the synthesis of the blue InP QDs using the TMSP, the issue is far from resolved because of their low PLQY (around 40%) along with emission at a greenish-blue light wavelength (over 488 nm).

Here, we demonstrate a synthetic method for engineering the core size of InP@ZnS core@shell QDs suitable for blue emission and unveil the associated significance of shell thickness and materials via first-principles simulations based on

Y.-H. Suh, S. Lee, S.-M. Jung, S. Y. Bang, J. Yang, X.-B. Fan, S. Zhan, C. Samarakoon, J.-W. Jo, Y. Kim, H. W. Choi, L. G. Occhipinti, T. H. Lee, D.-W. Shin, J. M. Kim
Electrical Engineering Division
Department of Engineering
University of Cambridge
9 JJ Thomson Avenue, Cambridge CB3 0FA, UK
E-mail: thl@knu.ac.kr; ds887@cam.ac.uk
T. H. Lee
School of Materials Science and Engineering
Kyungpook National University
Daegu 41566, South Korea
The ORCID identification number(s) for the author(s) of this article can be found under https://doi.org/10.1002/adom.202102372.

DOI: 10.1002/adom.202102372

density functional theory (DFT). This method benefits from the incipient ZnS (i-ZnS) complexes, namely, active shell-forming molecules pre-existing during the early stage of InP nucleation and growth. The growth of InP nuclei (synthesized by a quick hot injection of TMSP at 280 °C) is effectively suppressed by the i-ZnS, resulting in small InP core sizes around 1.8 nm. With an accompanying shell-growth process (additional shell coating), the synthesized InP@ZnS QDs show a blue emission (483 nm) with ≈52% PLQY and 49 nm of full width half maximum (FWHM). Variation of peak positions in X-ray photoelectron and Raman spectroscopies with shell formation indicates that the InP core in InP@ZnS QDs comes under the compressive force with the ZnS shell thickening. This experimental finding is verified by DFT simulations, which show the gradual thickening of ZnS (or ZnSe) shell gives rise to densification of InP core because of the compressive force induced by the lattice-constant difference between InP and ZnS (or ZnSe). The associated chemical, structural, and bandgap changes in the InP core region, along with their dependence on shell materials, are discussed in detail. All-solution-based QD LEDs (QLEDs) with the blue QDs as an emissive layer show a high luminance of 1162 cd m^{-2} and a maximized external quantum efficiency (EQE) of 1.4%.

2. Results and Discussion

The synthetic method for blue InP QDs utilizing i-ZnS complexes is schematically described in **Figure 1**A. The synthesis procedures are based on the hot-injection method with TMSP in a one-pot batch. The key strategy of our synthesis method is to form the i-ZnS complexes in solution before the injection of TMSP (viz. before the formation of InP nuclei). Initially, the mixture of indium and zinc precursors with various concentrations (0–0.3 mmol) of sulfur source (1-dodecanethiol, 1-DDT) is heated to 280 °C, the core growth temperature (see the methods in Supporting Information). The i-ZnS complexes stem from ZnS that are formed by the reaction between the sulfur source and zinc oleate ($C_{36}H_{66}O_4Zn$, $ZnOA_2$) upon heating. The formation of the complexes that could be in the form of [ZnS] monomer[19] or nanocluster[20,21] is evidenced by the emergence of an excitonic peak near 320 nm (Figure S1, Supporting Information). To initiate the formation of InP nuclei, TMSP, which exhibits high reactivity to indium precursors, is quickly injected into the hot solution that contains i-ZnS at 280 °C. In subsequent courses of InP nucleation and growth, the i-ZnS complexes may initiate chemical interactions with the atoms on the surface of the growing InP nuclei. We speculate that such passivation reactions play an essential role in restraining the crystal growth of the cores. As a result, the growth of the InP core is drastically suppressed by the presence of i-ZnS complexes, and the resultant final size of the InP core of QDs could become small enough to emit the blue light (Figure 1A). We refer to this initial shell coating by i-ZnS complexes as an early-stage shell coating (ESC), and the InP QDs after the ESC process are denoted as InP_{ESC} QDs. As a final step, an additional ZnS shell coating procedure (InP_{ESC}@ZnS QDs) is implemented to improve the stability and PLQY of QDs.

To understand the working principle of the ESC process, we characterized the absorbance and photoluminescence (PL) spectra of the QDs synthesized with the procedures outlined above. With 0 mmol of sulfur source in solution (the absence of ESC process), the peak emission wavelength of InP core-only QDs was at the green color region of ≈500 nm (green dot in Figure 1B), which is certainly insufficient for our purpose. To initiate the ESC process, 0.1 to 0.3 mmol of the sulfur source was added to the initial solution. We observed that the growth of the InP core of resultant QDs was then effectively suppressed, leading to PL peak emission wavelength located in the blue color region. A trend of gradual blue-shift with sulfur addition (from 491 nm [0.0 mmol] to 476 nm [0.3 mmol]) is observed, as shown in Figure 1C. Another consequence of the ESC process is that the PLQY increases from 14% to 27% as the InP core-only QDs transform to the InP_{ESC} QDs. The origin of the enhanced PLQY is ascribed to the passivation of surface defects of InP nuclei by i-ZnS complexes, which means the reduction of its non-radiative transition probability.

The ZnS shell of InP_{ESC} QDs is not thick enough to ensure chemical stability and high optical efficiency. To this end, an additional ZnS shell-growth procedure for the InP_{ESC} QDs (see the method, Supporting Information) was implemented to increase their shell thickness so as to enhance the QD stability and PLQY. After the additional ZnS shell coating, a slight red-shift of each peak wavelength of resultant QDs was observed; however, the trend of blue-shift with sulfur addition (522 nm [0.0 mmol] to 477 nm [0.3 mmol]) was still preserved, as shown in Figure 1D,E. The improvement of PLQY with the additional shell coating implicitly indicates that further passivation of surface defects of InP_{ESC} QDs is achieved (Figure 1E). The red-shifted emission could arise, in principle, because of either a further growth of the InP core of InP_{ESC} QDs during the additional shell coating, or a weakening of quantum confinement with shell thickening, or as a consequence of both of the effects. Specifically, with 0.1 mmol of sulfur source in solution (S poor, $Zn_{conc}/S_{conc} = 20$), the red-shifted peak emission ($(\lambda_{ESC,\ add\_S} - \lambda_{ESC}) / \lambda_{ESC} \times 100$, 2.5%) may mean that the ESC process is insufficient to prevent the overgrowth of the InP core during the additional shell coating. Also, the relatively low PLQY (43%) indicates that the synthesized InP_{ESC}@ZnS QDs seem to be still significantly influenced by non-radiative quenching sources, due to their insufficient shell thickness. On the other hand, with 0.3 mmol of sulfur source in solution (S rich, $Zn_{conc}/S_{conc} = 6.7$), a negligible red-shift in the peak emission wavelength (0.2%) is observed indicating successful and strong suppression of the core overgrowth. However, the relatively low PLQY (41%) was measured presumably due to the increasing interfacial defects between the core and shell layer with the formation of a thick ZnS shell.[22] A similar PLQY abatement was also observed even with higher sulfur concentrations in the solution ($Zn_{conc}/S_{conc} = 5$ and 4, not shown). With 0.2 mmol of sulfur source in solution ($Zn_{conc}/S_{conc} = 10$, red-shift, 0.6%), the empirically maximized PLQY of ≈ 52% at the peak wavelength of 483 nm was achieved. Also, we found that only 10 min of ESC process with 0.2 mmol of sulfur source (cf. ESC process for 60 min above) sufficed to complete InP_{ESC}@ZnS QDs with desired emission properties (Figure S2, Supporting Information). The optical bandgap of QDs was obtained according to

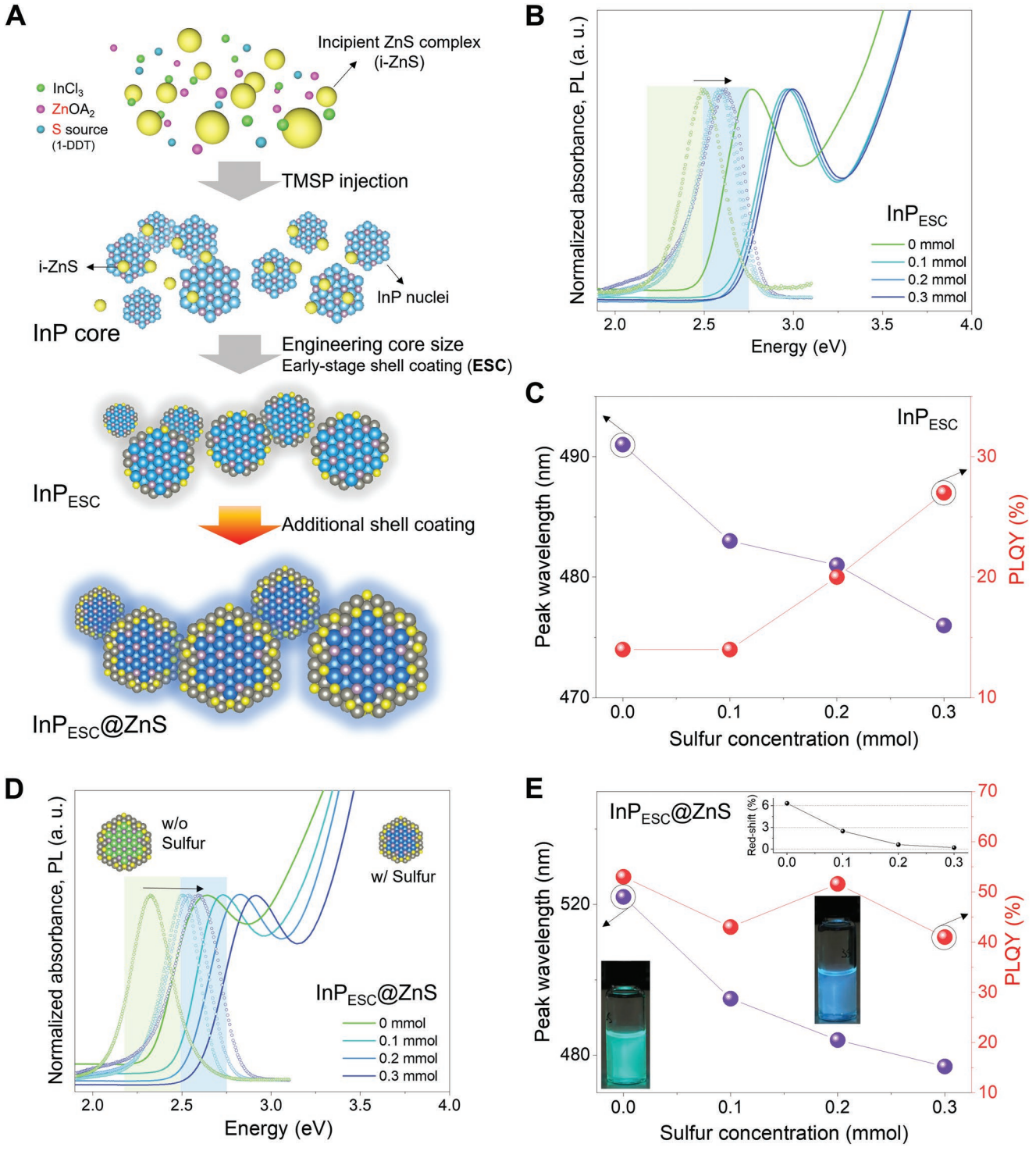

Figure 1. A) Schematic illustration of synthetic procedure of blue InP QDs. B) Optical properties and C) peak wavelength and PLQY (%) of blue InP_{ESC} QDs as a function of sulfur concentration. In the absence of the sulfur, the PL emission from InP cores was green in color. D) Optical properties and E) peak wavelength and PLQY (%) of blue InP_{ESC}@ZnS QDs after an additional shell coating as a function of sulfur concentration. The maximized PLQY was ≈52% at 483 nm with 49 nm of FWHM. The insets show photo images of InP@ZnS and InP_{ESC}@ZnS QDs in solution, and the red-shift of each peak wavelength as a function of sulfur concentration (upper right).

the Tauc plot (Figure S3 and Section S2, Supporting Information). The dependence of the bandgap on QD types will be discussed in more detail from DFT-based computational modeling. We further investigated that our proposed synthetic method can also be adopted for other sulfur chemicals, such as sulfur powder in trioctylphosphine (TOP) solvent (Figure S4,

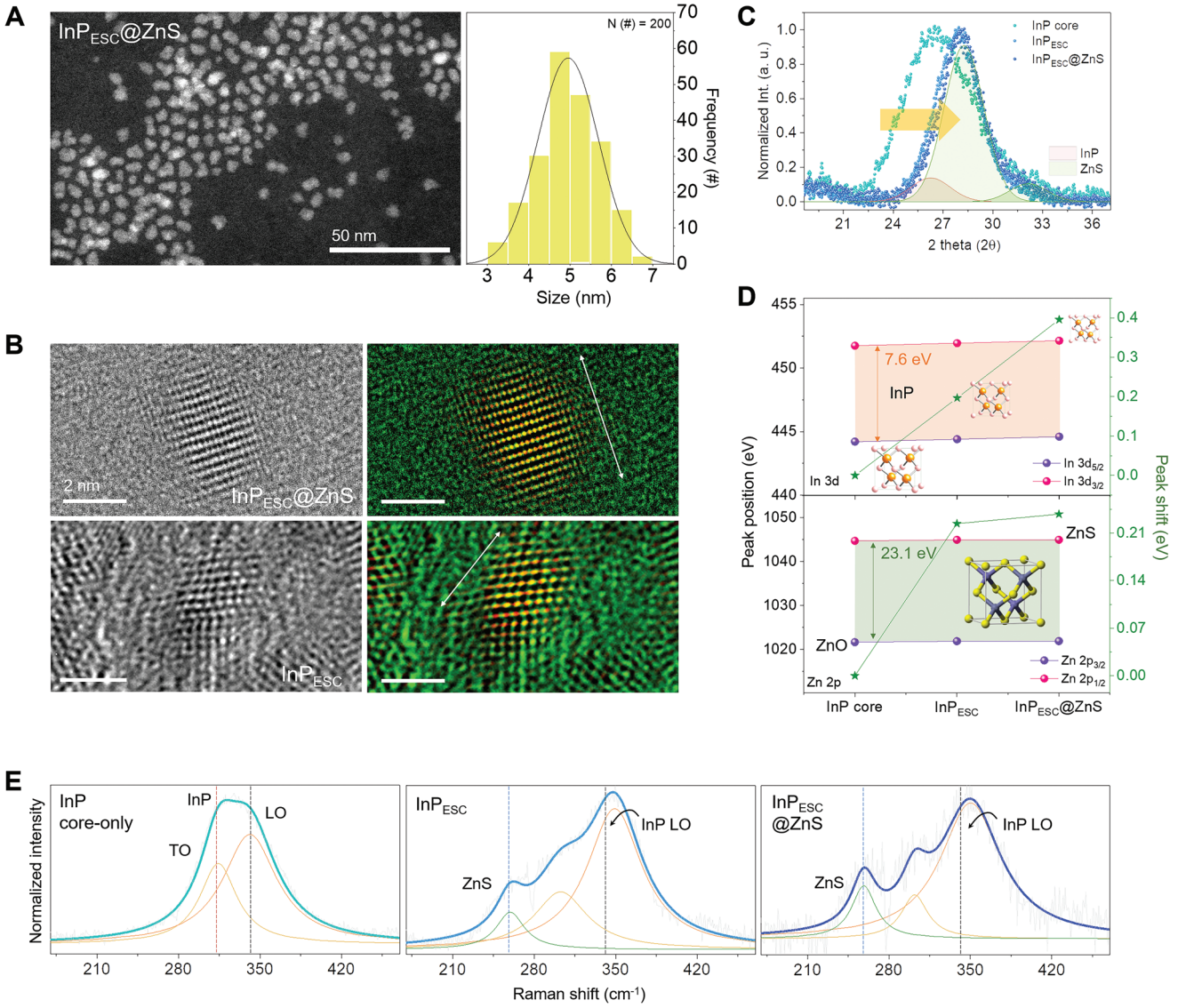

Figure 2. Size distributions and chemical and structural properties of InP core-only, InP$_{ESC}$, and InP$_{ESC}$@ZnS QDs. A) TEM image and histogram of InP$_{ESC}$@ZnS. The average size was 4.95 ± 0.75 nm. B) HRTEM images and FFT filtered images of InP$_{ESC}$@ZnS and InP$_{ESC}$ QD. C) Variation of XRD patterns with the formation of ZnS shell. D) High-resolution XPS profiles of In 3d and Zn 2p. The inset shows the atomic positions for the cubic zinc blende phase of InP and ZnS. E) Raman spectra at an excitation energy of 2.41 eV. The LO and TO of InP core-only QDs and the Raman shift at ≈260 cm^{-1} for the ZnS shell formation (InP$_{ESC}$ and InP$_{ESC}$@ZnS QDs).

Supporting Information). The formation of i-ZnS complexes along with similar effects of ESC procedure was confirmed through the absorbance and PL spectra of QDs synthesized with sulfur powder in TOP.

The structural properties of synthesized blue QDs (with or without ESC process with 0.2 mmol sulfur source) were studied by transmission electron microscopy (TEM), X-ray photoelectron spectroscopy (XPS), Raman spectroscopy, and X-ray powder diffraction (XRD). The sizes of QDs were directly counted from dark-field TEM images (**Figure 2**A and Figure S5, Supporting Information). The measured sizes of InP core-only, InP$_{ESC}$, and InP$_{ESC}$@ZnS QDs were 3.25 ± 0.38, 3.04 ± 0.38, and 4.95 ± 0.73 nm, respectively. Interestingly, the average size of the InP$_{ESC}$ QD is smaller than that of the InP core-only QDs, even though the InP$_{ESC}$ QDs have a thin ZnS shell formed by the ESC process. This observation supports our argument that the ESC process plays a role in preventing the overgrowth of InP cores. We estimated the average InP core size of InP$_{ESC}$@ZnS to be ≈1.8 nm through EDS line profile (Figure S6, Supporting Information). The relative standard deviations in size for InP core-only, InP$_{ESC}$, and InP$_{ESC}$@ZnS QDs were 11.7%, 12.5%, and 14.7%, respectively, revealing a broader size distribution as the ZnS thickness increased. Figure 2B shows the HRTEM and its filtered images of InP$_{ESC}$@ZnS (upper panel) and InP$_{ESC}$ (lower panel) QDs (QD: yellow, background: green). The filtered images were obtained after masking the selected QD by using fast Fourier transform (FFT). We observed atomically resolved individual QDs, indicative of high crystallinity. Even

if the structure of inner InP cores was unidentifiable in this image due to the presence of a shell, the shell was identified as a zinc blende ZnS with a lattice spacing of 3.07 Å, which corresponds to the lattice spacing between (111) planes (Figure S7, Supporting Information).

The XRD patterns for InP core-only, InP_{ESC}, and InP_{ESC}@ZnS QDs confirm the crystallinity of QDs (Figure 2C; Figure S8, Supporting Information). The zinc-blende phase of the InP core and ZnS shell for all the prepared QDs is verified through the comparison with published JCPDS: 00-032-0452 (InP) and JCPDS: 01-080-0020 (ZnS), respectively, in agreement with the conclusion from TEM and XPS data. The XRD peak positions of InP core-only QDs correspond to those of the cubic zinc-blende phase of bulk InP with a dominant contribution from the (111) crystal plane, along with a broadened FWHM due to a relatively low crystallinity of InP core-only QDs. With the passivation of i-ZnS complexes on the InP core-only QDs, the XRD peak positions suddenly approach those of the cubic zinc-blende phase of ZnS with a dominant contribution from the (111) crystal plane (together with a small participation of the InP (111) plane contribution).[18,23] At the same time, the FWHMs of the peaks become narrowed.

The energies and intensities of photoelectron peaks in XPS data enable the identification of the composition of the synthesized QDs (Figure 2D). The In 3d peaks of InP core-only QDs were located at 444.20 eV (In $3d_{5/2}$) and 451.80 eV (In $3d_{3/2}$) with a spin-orbit splitting (SOS) of 7.6 eV, indicative of In(III) state.[24] While the SOS remained constant, the binding-energy (BE) difference (ΔBE, $P_{BE} - P_{InP\ core}$) was found to be + 0.2 or + 0.4 eV for InP_{ESC} or InP_{ESC}@ZnS QDs, respectively (Figure S9, Supporting Information). Theoretically, initial state contributions to ΔBE that arise from lattice strain (e.g., change of nearest interatomic distance) will be largest for 3d series transition metals,[25,26] and the observed positive ΔBE of In 3d peaks, for example, the shift toward a higher BE, is likely to be a consequence of lattice compression. We note that the InP core comes to be under a compressive force induced by the successive formation of ZnS shell during the ESC process and subsequent, additional ZnS shell coating process. The compressive force becomes stronger, as the ZnS shell thickness increases (see the InP unit cell with a zinc blende phase in the inset of Figure 2D), which will be explained in detail from the DFT modeling. The energy level of Zn 2p in InP core-only QDs is split into Zn $2p_{3/2}$ (1021.6 eV) and Zn $2p_{1/2}$ (1044.7 eV) with the SOS of 23.1 eV, which can be assigned to the Zn(II) state.[27] Without sulfur source (0.0 mmol), the formation of ZnO with a zinc wurtzite phase (see XRD pattern in Figure S10, Supporting Information) was identified, which is evidenced by the lower BE than that of ZnS (+0.22 eV) with a zinc blende phase.[28] The high-resolution XPS spectra of P 2p and S 2p in InP_{ESC}@ZnS QDs show the formation of core@shell structure without any distinct surface defects identified (Figure S11, Supporting Information).

The transverse and longitudinal optical modes (TO and LO)[29] for InP core-only, InP_{ESC}, and InP_{ESC}@ZnS QDs were obtained by the Raman spectra (Figure 2E). Both of the TO (314.2 cm^{-1}) and LO (341.2 cm^{-1}) modes for the InP core-only QDs were clearly observed, whose values precisely correspond to those for the InP nanocrystals.[29] With increasing ZnS shell thickness, that is, the transition from an InP_{ESC} to InP_{ESC}@ZnS QD, the original LO peak of InP core in each QD was slightly broadened along with the shift to higher frequencies. The broadened InP LO stems from ZnS LO that has a similar vibrational frequency to that of the InP LO around 350 cm^{-1}.[30] LO frequencies of InP_{ESC} and InP_{ESC}@ZnS QDs are located at higher frequencies than the LO of InP core-only QDs because of the compressive force on the InP core lattice with the increase of ZnS shell thickness.[31] The Raman intensity at 259 cm^{-1} for ZnS[32] was gradually enhanced due to the increased ZnS shell thickness.

To understand the experimental findings on the emission wavelength shift and the emergence of compressive force exerted upon InP core arising with ZnS shell thickening, we employed the DFT-based first-principles simulations. To mimic the synthesized QDs (viz. InP core-only, InP_{ESC} (or ESC), and InP_{ESC}@ZnS QDs), we simulated three types of QD models for each shell material by successively adding a shell layer on the surface of the InP core-only QD (**Figure 3**A). Zinc selenide (ZnSe), which is widely utilized as an intershell or gradient shell for InP QDs[33] was also simulated to verify which shell materials fit the blue emission. The first shell layer partially covers the InP core-only model, in consideration of the experimental finding that the ESC process may not fully passivate the surface defect states of InP cores. Considering the partial valence charges involved in covalent bonding for each atomic species, fictitious hydrogen atoms with appropriate partial charges passivated the surface elements.[34] The QD models, generated in this way, showed an XRD peak shift with shell coating (Figure S12, Supporting Information), in agreement with experimental findings (Figure 2C), which may be, in turn, the simulational verification of shell formation of synthesized QDs.

The interatomic distance between In and P atoms decreased with the growth of both shell materials (Figure S13, Supporting Information), which is indicative of altered chemical interactions at the InP core with shell formation. The quantum theory of atoms in molecules[35] approach was then employed to investigate the nature of chemical bonds for the InP core part of each QD model. Figure 3B shows charge densities at the bond critical points (ρ_{bcp}) for neighboring In-P pairs. The observed increase in ρ_{bcp} with shell growth can be understood as a result of enhanced covalency of the InP core part with shell formation. Moreover, the reduced charge transfer from In to P atoms (Figure 3C) observed at the same time with the increase of ρ_{bcp} implies that the enhancement of covalency arises at the expense of ionicity. A meaningful dependence on shell materials exists such that a more significant reduction (or increment) in interatomic distances (or ρ_{bcp}) is found for ZnS than ZnSe. We also investigated the impact of shell formation on the atomic (Bader) volume,[36] which can be considered as a measure of the inverse of local atomic density. The average atomic volume for In and P atoms (Figure 3D) diminished, in common, pointing to the increment of InP-core density with shell formation (Figure 3E). Interestingly, it was found that a larger atomic volume was observed near the surface of InP core-only QD than at the core center, but precisely the opposite trend was observed for core@shell QDs (Figure 3F,G). As a result, the InP core is subjected to a compressive force with shell coating due to the smaller lattice constant of ZnS (or ZnSe) compared to that of InP.[31]

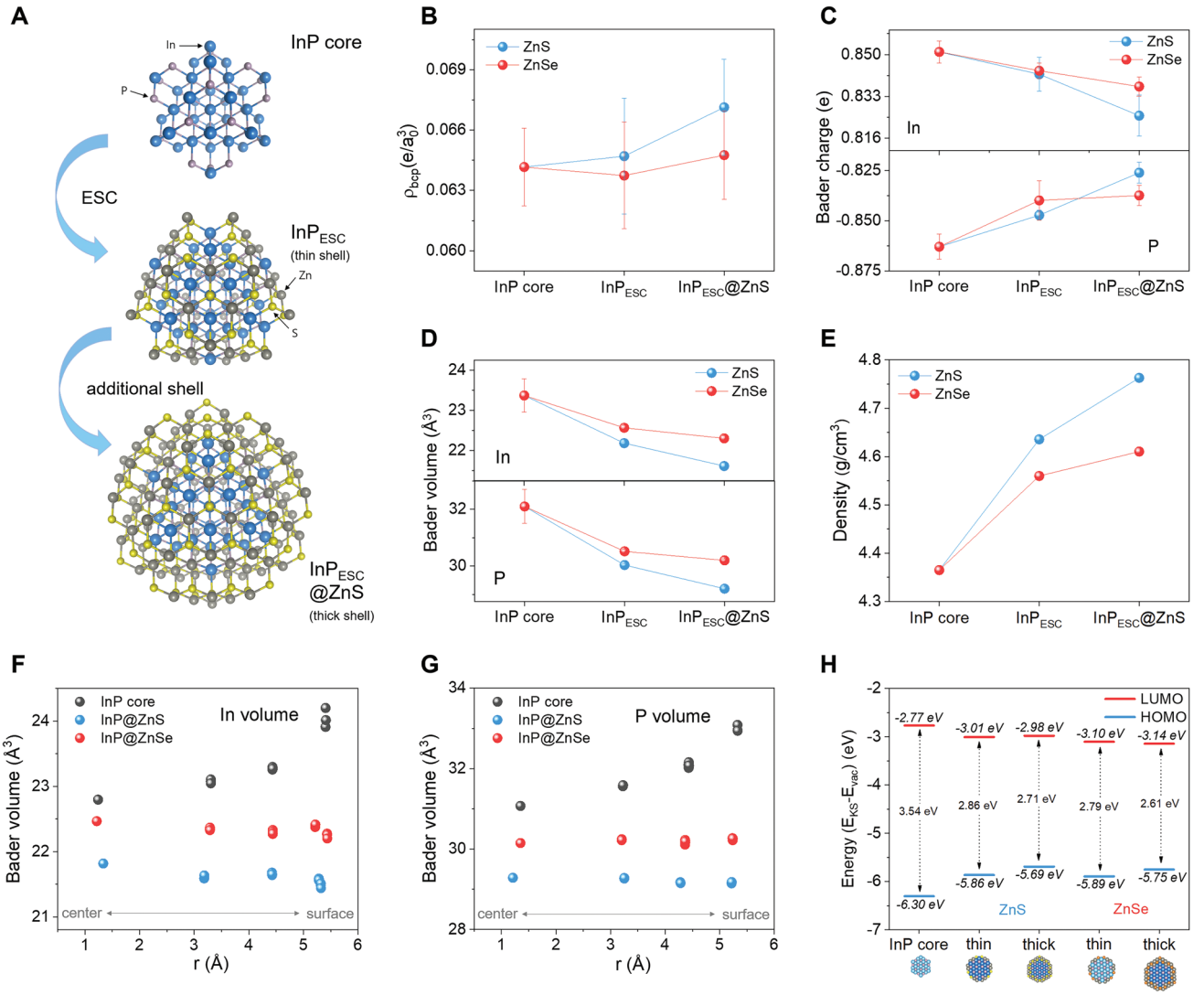

Figure 3. DFT-based first-principles modeling. A) InP core-only, InP$_{ESC}$, and InP$_{ESC}$@ZnS models. B) Charge density at bond critical point (ρ_{bcp}) of InP core part of each QD model. C) Bader charge of In and P. D) Bader volume of In and P with shell formation. E) InP core density as a function of the thickness of ZnS (or ZnSe) shell. F,G) Variation of Bader volume of In (F) and P (G) in each QD model. H) HOMO and LUMO energy levels calculated from the DFT calculation. A larger reduction in bandgap is observed with the formation of ZnSe shell than ZnS shell.

The magnitude of the compressive force becomes stronger as the shell thickness increases, and more significant compression is being developed with ZnS shell than ZnSe shell because of relatively larger lattice mismatch of ZnS (7.7%) compared to that of ZnSe (3.5%). The amount of compressive force was relatively larger near the core@shell interfaces than at the core center (Figure 3F,G). Hence, it is legitimate to anticipate that lattice defects, such as vacancies, are most likely to form at core@shell interfaces to reduce the compressive forces being developed with shell coating. In this respect, the decreased PLQY with high sulfur source concentrations (>0.2 mmol) for the ESC process may be attributed to the enhanced non-radiative transition rate due to the defects at the core@shell interfaces with a growing shell.[22]

Figure 3H shows the energy levels of the highest occupied molecular orbital (HOMO) and lowest unoccupied molecular orbital (LUMO) calculated for all the QD models studied here. The apparent observations are that: i) as the size of InP core increases, the bandgap decreases (Figure S14, Supporting Information); ii) with the increment of shell thickness, the bandgap is narrowed; iii) the thickening of the ZnSe shell induces a sharper drop in bandgap than does the ZnS shell (Figure S15, Supporting Information). All these observations exactly correspond to the trends observed in the experiment (Figure 1), and their origins are, in principle, ascribed to the weakening of quantum confinement effect with either the increase of InP core size (for (i))[37] or the delocalization of InP-core states to the shell volume (for (ii)).[38] Stronger delocalization into the ZnSe shell than the ZnS shell, due to a smaller band-gap difference, results in (iii).[38,39] It is noteworthy that these rather conventional explanations do not consider a possible impact of the density change with shell formation (as shown in Figure 3E) on the bandgap. To study this, we separated the InP-core part of each core@shell QD model and calculated its bandgap without

any structural relaxations to preserve its core structure, as it was in the original core@shell QD (Figure S16, Supporting Information). The bandgap of the InP cores in each core@shell QD shows a gradual increase with shell thickening. This trend was evident for the ZnS shell, yet less significant for the ZnSe shell. This result coincided with the trend found in bulk InP with varying densities (Figure S17, Supporting Information). Therefore, the decrease in bandgap with shell coating is the result of two opposing contributions of band-gap widening due to the core densification, and of the bandgap narrowing induced by the delocalization of InP-core states. In this respect, the ZnS shell, which produces a denser InP core and stronger quantum confinement (as observed in the experiment with the application of the ESC process), provides more plausible conditions for the shorter-wavelength (blue in this case) emission, as observed in the experiment.

A 3D schematic illustration of the device structure of solution-based InP_{ESC}@ZnS QLED is shown in **Figure 4**A. The blue QLED consists of poly(3,4-ethylenedioxythiophene) polystyrene sulfonate (PEDOT:PSS) as a hole injection layer, poly(9,9-dioctylfluorene-*co*-*N*-(4-butyl-phenyl)diphenylamine) (TFB) as a hole transport layer, QD as an emissive layer, zinc magnesium oxide (ZnMgO) as an electron transport layer, and aluminum as a cathode layer (Figure 4A,B) on a pixelated indium thin oxide glass, as an anode. To improve the charge recombination efficiency, we selected each component material based on its electronic structure (Figure 4B).[40] The time-correlated single-photon counting, along with electroluminescence (EL) spectra of their QLEDs, was measured to understand the probability of radiative recombination of all the synthesized QDs films (Figure 4C). The PL decay curves of the InP core-only, InP_{ESC}, and InP_{ESC}@ZnS QDs were fitted well to tri-exponential functions. An average lifetime of 10.1, 25.3, and 56.0 ns was obtained (Figure S18, Supporting Information). The progressive increase in the average PL lifetimes of QDs with a thicker ZnS shell arises because of the decrease of electron (or hole) trapping of excitons by the surface defect states and/or the suppressed Förster energy transfer between the QDs, both of which effectively diminish non-radiative transitions.[41] We note that the additional shell-formation process helps enhance the radiative electron–hole recombination with higher PLQY (Figure S18, Supporting Information).[42] This observation is in agreement with the result of the bottom panel in Figure 4C that strong blue EL is observed only from InP_{ESC}@ZnS QLEDs (cf. the violet light emitting from the TFB with small EL of InP core-only or InP_{ESC} QDs in QLEDs). The blue InP_{ESC}@ZnS QLED shows a maximum EQE of 1.4% (Figure S19, Supporting Information, good reproducibility with an average EQE of 1.03 ± 0.18%). In current density–voltage–luminance (*J*–*V*–*L*) curve, the luminance consistently increased with increasing operating voltage, reaching 1162 cd m^{-2} at 6.4 V with a current density of 447.7 mA cm^{-2} (Figure 4D, the photoimage of blue-light emission at 6 V). In addition, we predicted a *J*–*V*–*L* curve based on the charge transport model,[43,44] which is consistent with the experimental curve. All the blue EL peak positions of the QLED with voltages ranging from 3.6 to 6 V remain constant at 487 nm, indicating that the EL spectrum is independent of applied voltage (Figure 4E).[45,46] Furthermore, we observed

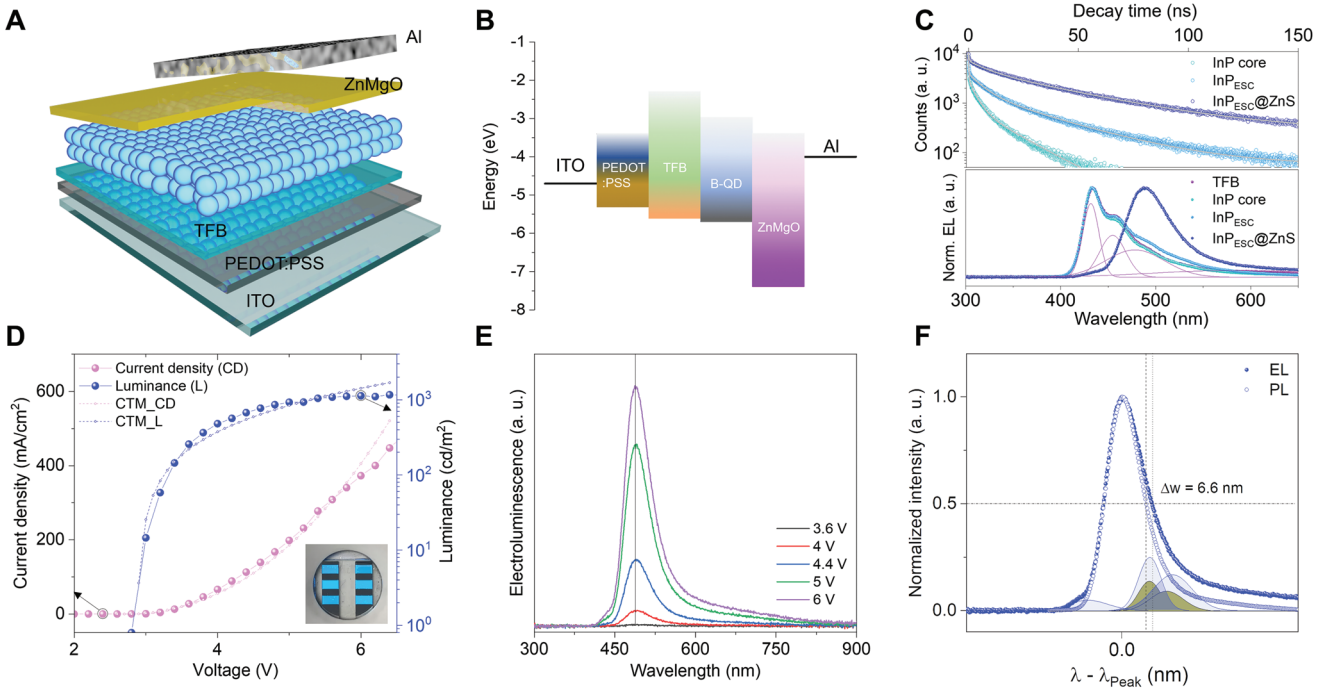

Figure 4. EL characteristics of InP_{ESC}@ZnS. A) Schematic of the device structure and B) the corresponding energy band diagram. C) PL decay curves and EL spectra of QLEDs of InP core-only, InP_{ESC}, and InP_{ESC}@ZnS QDs. D) Current density-voltage-luminance curve of the device and simulated curves by the charge transport model (CTM). The maximum luminance of 1162 cd m^{-2} was observed. The inset shows the captured photo image of blue-light emission from the devices at 6 V. E) EL spectra of a QLED at increasing operating voltages. F) Comparison between EL and PL spectra for InP_{ESC}@ZnS QDs. The defect-associated long-wavelength emissions appear more evidently in the EL than in the PL, resulting in an increased FWHM of EL spectrum by 6.6 nm.

that the EL spectrum of blue InP_{ESC}@ZnS QLEDs exhibits a red-shift (4–7 nm) and a slight broadening in FWHM (6.6 nm), compared with the PL spectrum of QDs in solution (Figure 4F). Such differences may be attributed to the interdot interactions in close-packed solid film, dielectric dispersion, intrinsic defects, or the electric field-induced Stark effect.[12]

3. Conclusion

In summary, the InP_{ESC}@ZnS QDs for blue emission were realized through an ESC process developed in this study, from which the InP core size can be effectively controlled. The i-ZnS complexes, pre-existing in a one-pot batch solution before InP core growth, play essential roles during the ESC process: i) forming a shell on the InP cores (viz. the formation of InP_{ESC} QDs), while diminishing surface defects by passivating dangling bonds on the core surface, and ii) suppressing the overgrowth of InP cores, thereby facilitating the formation of small InP cores for blue-luminant QDs. The subsequent, additional ZnS shell coating resulted in InP_{ESC}@ZnS QDs with high optical efficiencies and chemical stability. The working principle on the ESC process is revealed by investigating chemical and structural characteristics of InP QDs with the aid of the DFT modeling. The electronic structure of blue InP_{ESC}@ZnS QDs investigated by DFT shows a strong dependence on the densification of InP core and weakening of quantum confinement effect with shell coating. Finally, blue QLEDs with InP_{ESC}@ZnS QDs show a peak EQE of 1.4% and a high luminescence of 1162 cd m^{-2}.

Supporting Information

Supporting Information is available from the Wiley Online Library or from the author.

Acknowledgements

Y.-H.S. and S.L. contributed equally to this work.

Conflict of Interest

The authors declare no conflict of interest.

Data Availability Statement

The data that support the findings of this study are available from the corresponding author upon reasonable request.

Keywords

blue emission, density functional theory modeling, incipient ZnS, indium phosphide quantum dots, quantum dot light-emitting diodes

Received: November 2, 2021
Revised: January 5, 2022
Published online:

[1] P. Reiss, M. Carriere, C. Lincheneau, L. Vaure, S. Tamang, *Chem. Rev.* **2016**, *116*, 10731.
[2] J. Owen, L. Brus, *J. Am. Chem. Soc.* **2017**, *139*, 10939.
[3] Y. E. Panfil, M. Oded, U. Banin, *Angew. Chem. Int. Ed. Engl.* **2018**, *57*, 4274.
[4] M. V. Kovalenko, L. Manna, A. Cabot, Z. Hens, D. V. Talapin, C. R. Kagan, V. I. Klimov, A. L. Rogach, P. Reiss, D. J. Milliron, P. Guyot-Sionnnest, G. Konstantatos, W. J. Parak, T. Hyeon, B. A. Korgel, C. B. Murray, W. Heiss, *ACS Nano* **2015**, *9*, 1012.
[5] H. Moon, C. Lee, W. Lee, J. Kim, H. Chae, *Adv. Mater.* **2019**, *31*, 1804294.
[6] K. Wu, T. Lian, *Chem. Soc. Rev.* **2016**, *45*, 3781.
[7] J. Yang, M. K. Choi, D. H. Kim, T. Hyeon, *Adv. Mater.* **2016**, *28*, 1176.
[8] Y. Kim, S. Ham, H. Jang, J. H. Min, H. Chung, J. Lee, D. Kim, E. Jang, *ACS Appl. Nano Mater.* **2019**, *2*, 1496.
[9] Y. H. Won, O. Cho, T. Kim, D. Y. Chung, T. Kim, H. Chung, H. Jang, J. Lee, D. Kim, E. Jang, *Nature* **2019**, *575*, 634.
[10] H. J. Byun, J. C. Lee, H. Yang, *J. Colloid Interface Sci.* **2011**, *355*, 35.
[11] S. Xu, J. Ziegler, T. Nann, *J. Mater. Chem.* **2008**, 18, 2653.
[12] P. Ramasamy, K.-J. Ko, J.-W. Kang, J.-S. Lee, *Chem. Mater.* **2018**, *30*, 3643.
[13] J. Ning, U. Banin, *Chem. Commun.* **2017**, *53*, 2626.
[14] E. Ryu, S. Kim, E. Jang, S. Jun, H. Jang, B. Kim, S.-W. Kim, *Chem. Mater.* **2009**, *21*, 573.
[15] X. Yang, D. Zhao, K. S. Leck, S. T. Tan, Y. X. Tang, J. Zhao, H. V. Demir, X. W. Sun, *Adv. Mater.* **2012**, *24*, 4180.
[16] P. Ramasamy, N. Kim, Y.-S. Kang, O. Ramirez, J.-S. Lee, *Chem. Mater.* **2017**, *29*, 6893.
[17] K. Lim, H. S. Jang, K. Woo, *Nanotechnology* **2012**, *23*, 485609.
[18] T. Kim, S. W. Kim, M. Kang, S.-W. Kim, *J. Phys. Chem. Lett.* **2012**, *3*, 214.
[19] C. Xia, N. Winckelmans, P. T. Prins, S. Bals, H. C. Gerritsen, C. de Mello Donegá, *J. Am. Chem. Soc.* **2018**, *140*, 5755.
[20] A. L. Abdelhady, M. A. Malik, P. O'Brien, *J. Inorg. Organomet. Polym. Mater* **2014**, *24*, 226.
[21] S. H. Choi, K. An, E. G. Kim, J. H. Yu, J. H. Kim, T. Hyeon, *Adv. Funct. Mater.* **2009**, *19*, 1645.
[22] B. Ji, Y. E. Panfil, N. Waiskopf, S. Remennik, I. Popov, U. Banin, *Nat. Commun.* **2019**, *10*, 2.
[23] L. Li, P. Reiss, *J. Am. Chem. Soc.* **2008**, *130*, 11588.
[24] S. Kundu, N. N. Halder, P. Biswas, D. Biswas, P. Banerji, R. Mukherjee, S. Chakraborty, *Appl. Phys. Lett.* **2012**, *101*, 212108.
[25] P. S. Bagus, A. Wieckowski, H. Freund, *Comput. Theor. Chem.* **2012**, *987*, 22.
[26] A. Theodosiou, B. F. Spencer, J. Counsell, A. N. Jones, *Appl. Surf. Sci.* **2020**, *508*, 144764.
[27] T. J. Macdonald, D. D. Tune, M. R. Dewi, J. C. Bear, P. D. McNaughter, A. G. Mayes, W. M. Skinner, I. P. Parkin, J. G. Shapter, T. Nann, *J. Mater. Chem. C* **2016**, *4*, 3379.
[28] F. Wang, J. Liu, Z. Wang, A.-J. Lin, H. Luo, X. Yu, *J. Electrochem. Soc.* **2011**, *158*, H30.
[29] M. J. Seong, O. I. Mićić, A. J. Nozik, A. Mascarenhas, H. M. Cheong, *Appl. Phys. Lett.* **2003**, *82*, 185.
[30] M. Dimitrievska, H. Xie, A. Jackson, X. Fontané, M. Espíndola-Rodríguez, E. Saucedo, A. Pérez-Rodríguez, A. Walsh, V. Izquierdo-Roca, *Phys. Chem. Chem. Phys.* **2016**, *18*, 7632.
[31] M. Rafipoor, H. Tornatzky, D. Dupont, J. Maultzsch, M. D. Tessier, Z. Hens, H. Lange, *J. Chem. Phys.* **2019**, *151*, 154704.
[32] Z. Li, M. Chen, Q. Zhang, J. Qu, Z. Ai, Y. Li, *Appl. Clay Sci.* **2017**, *144*, 115.
[33] D. W. Shin, Y. H. Suh, S. Lee, B. Hou, S. D. Han, Y. Cho, X. B. Fan, S. Y. Bang, S. Zhan, J. Yang, *Adv. Opt. Mater.* **2020**, *8*, 1901362.
[34] X. Huang, E. Lindgren, J. R. Chelikowsky, *Phys. Rev. B* **2005**, *71*, 165328.
[35] R. F. W. Bader, *Acc. Chem. Res.* **1985**, *18*, 9.

[36] M. Yu, D. R. Trinkle, *J. Chem. Phys.* **2011**, *134*, 064111.
[37] A. P. Alivisatos, *Science* **1996**, *271*, 933.
[38] B. O. Dabbousi, J. RodriguezViejo, F. V. Mikulec, J. R. Heine, H. Mattoussi, R. Ober, K. F. Jensen, M. G. Bawendi, *J. Phys. Chem. B* **1997**, *101*, 9463.
[39] M. D. Tessier, D. Dupont, K. De Nolf, J. De Roo, Z. Hens, *Chem. Mater.* **2015**, *27*, 4893.
[40] H. Moon, W. Lee, J. Kim, D. Lee, S. Cha, S. Shin, H. Chae, *Chem. Commun.* **2019**, *55*, 13299.
[41] G. Devatha, S. Roy, A. Rao, A. Mallick, S. Basu, P. P. Pillai, *Chem. Sci.* **2017**, *8*, 3879.
[42] F. Purcell-Milton, A. K. Visheratina, V. A. Kuznetsova, A. Ryan, A. O. Orlova, Y. K. Gun'ko, *ACS Nano* **2017**, *11*, 9207.
[43] B. Kumar, S. A. Campbell, P. Paul Ruden, *J. Appl. Phys.* **2013**, *114*, 044507.
[44] F. Vahabzad, A. Rostami, M. Dolatyari, G. Rostami, I. Amiri, *Phys. B (Amsterdam, Neth.)* **2019**, *574*, 411667.
[45] E. Khodabakhshi, B. Klöckner, R. Zentel, J. J. Michels, P. W. Blom, *Mater. Horiz.* **2019**, *6*, 2024.
[46] Y. Shirasaki, G. J. Supran, W. A. Tisdale, V. Bulović, *Phys. Rev. Lett.* **2013**, *110*, 217403.